Supplementary Information

1 Supplementary figures

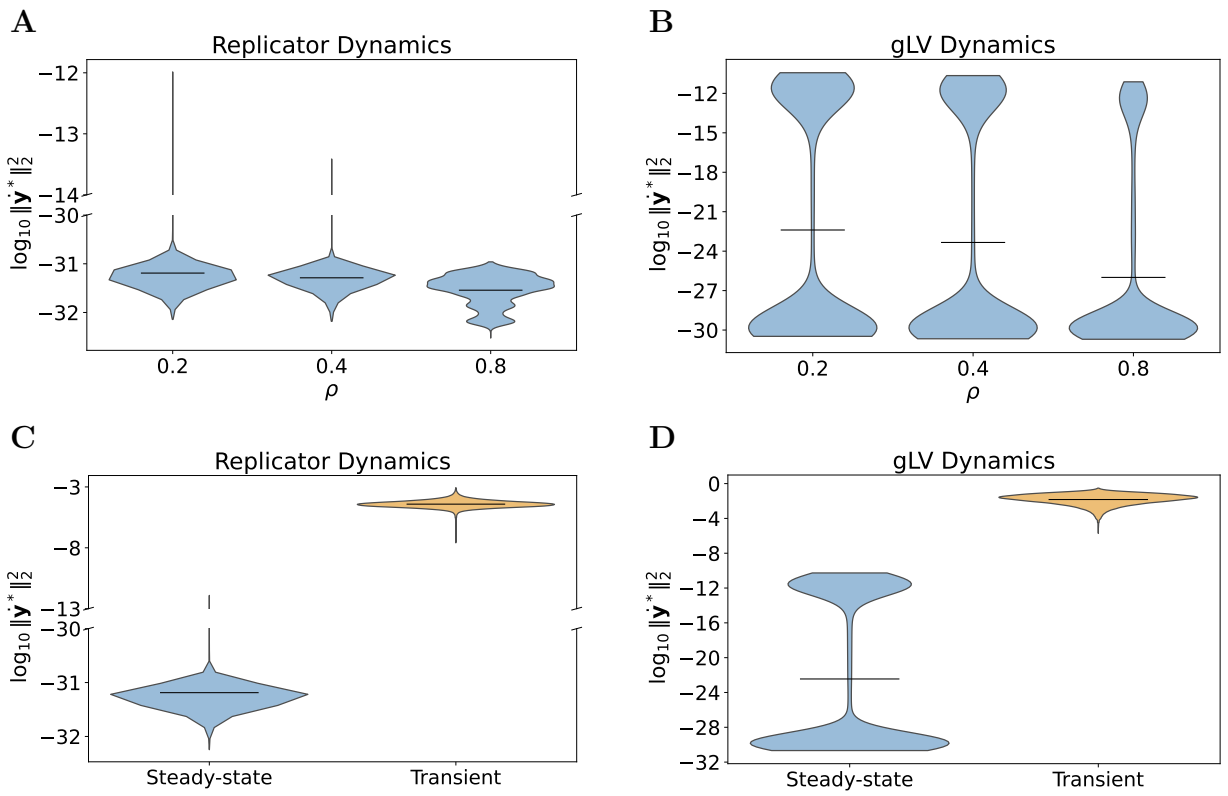

Figure S1: Distribution of $\log_{10}\|\dot{\mathbf{y}}^*\|_2^2$ for cross-sectional samples under replicator and gLV dynamics. (A, B) Long-time cross-sectional samples under interaction sparsity levels $\rho \in \{0.2, 0.4, 0.8\}$. (C, D) Comparison between steady-state versus transient samples. Lower values indicate samples closer to steady-state.

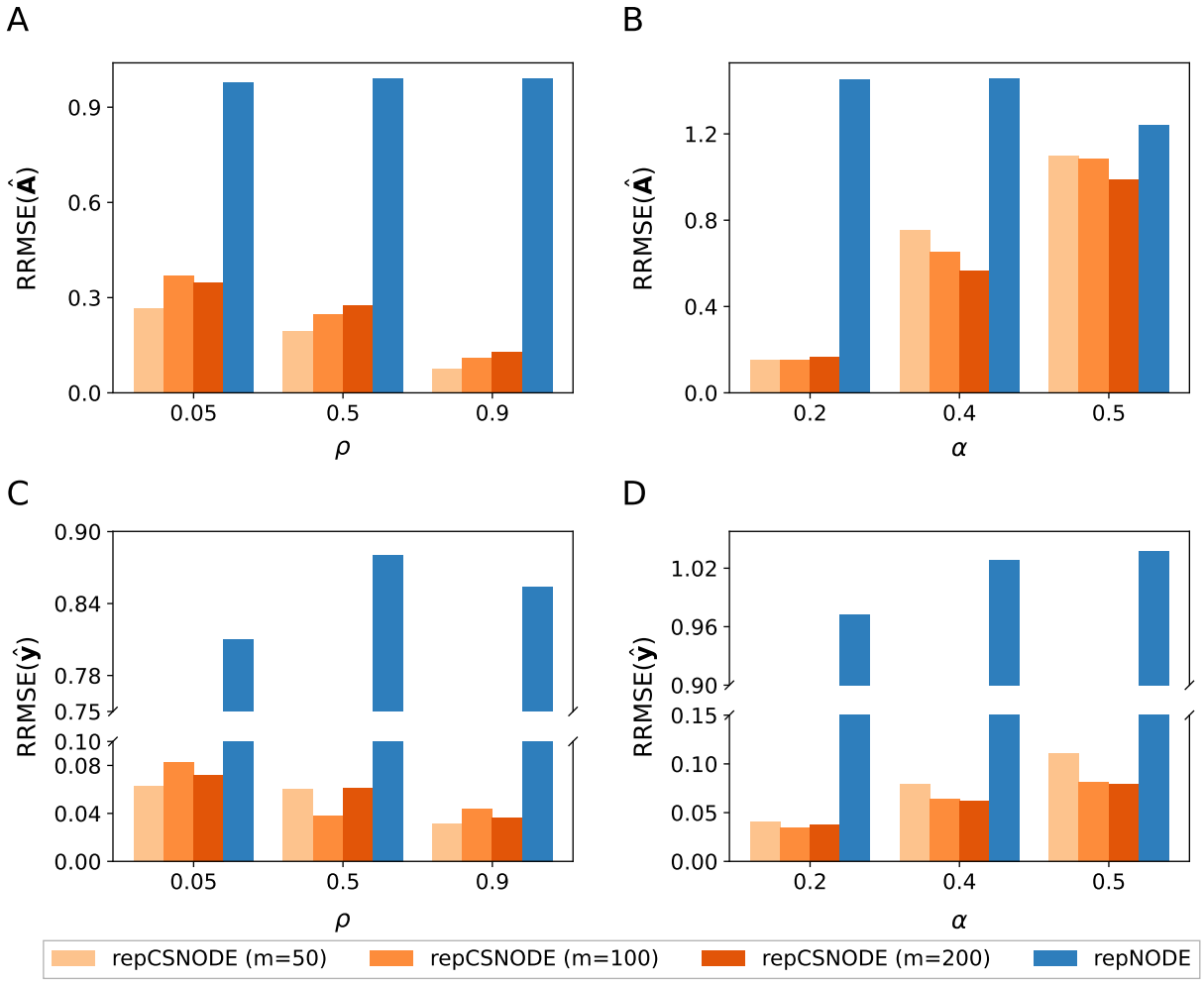

Figure S2: Performance comparison between repCSNODE and repNODE across a broad range of sparsity and noise settings for relative abundances. (A, C) Simulated datasets with fixed $\alpha = 0.05$ and $\eta = 0.01$, while varying ρ over $\{0.05, 0.5, 0.9\}$. (B, D) Simulated datasets with fixed $\rho = 0.2$ and $\eta = 0.01$, while varying α over $\{0.2, 0.4, 0.5\}$. Panels A and B show the mean RRMSE for interaction parameter estimation, and Panels C and D show the mean RRMSE for trajectory prediction. For repCSNODE, results are further stratified by the number of cross-sectional samples $m \in \{50, 100, 200\}$.

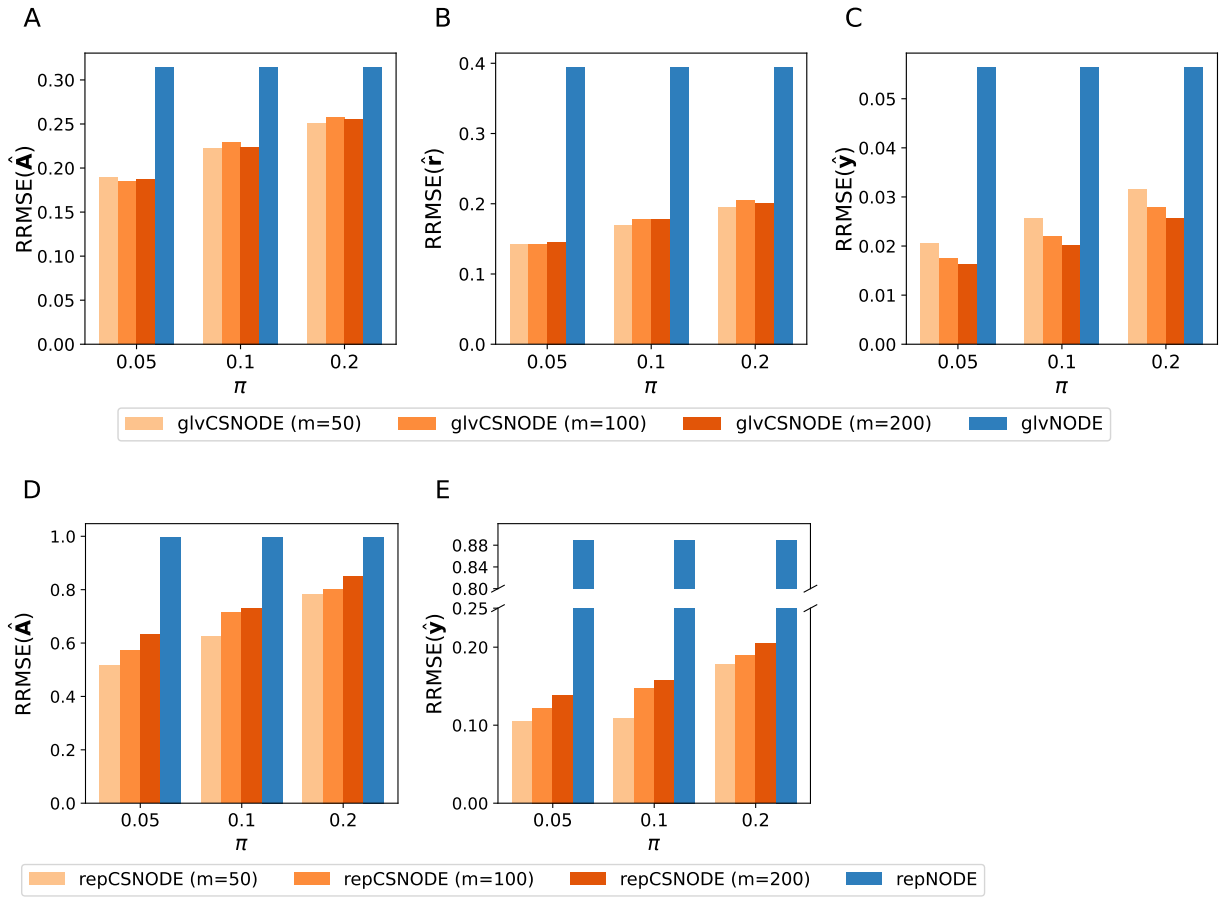

Figure S3: Performance comparison under simulation settings with sparse perturbations. Simulated datasets were generated with fixed $\alpha = 0.05$ and $\rho = 0.6$, while varying the activation probability π over $\{0.05, 0.1, 0.2\}$. Panels (A)–(C) compare glvCSNODE and glvNODE, and panels (D)–(E) compare repCSNODE and repNODE. For the CSNODE-based methods, results are further stratified by the number of cross-sectional samples $m \in \{50, 100, 200\}$.

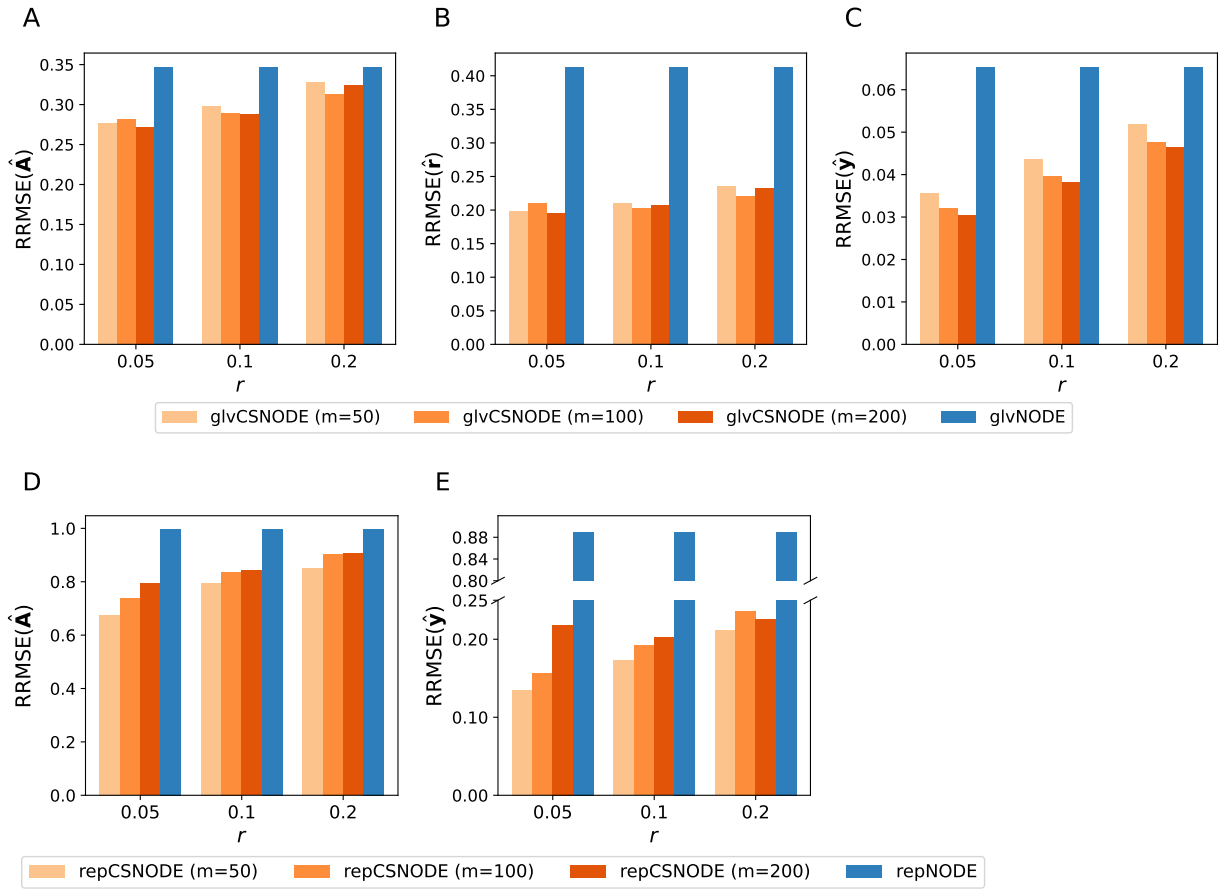

Figure S4: Performance comparison under simulation settings with sign-flip perturbations. Simulated datasets were generated with fixed $\alpha = 0.05$ and $\rho = 0.6$, while varying the flip probability r over $\{0.05, 0.1, 0.2\}$. Panels (A)–(C) compare glvCSNODE and glvNODE, and panels (D)–(E) compare repCSNODE and repNODE. For the CSNODE-based methods, results are further stratified by the number of cross-sectional samples $m \in \{50, 100, 200\}$.

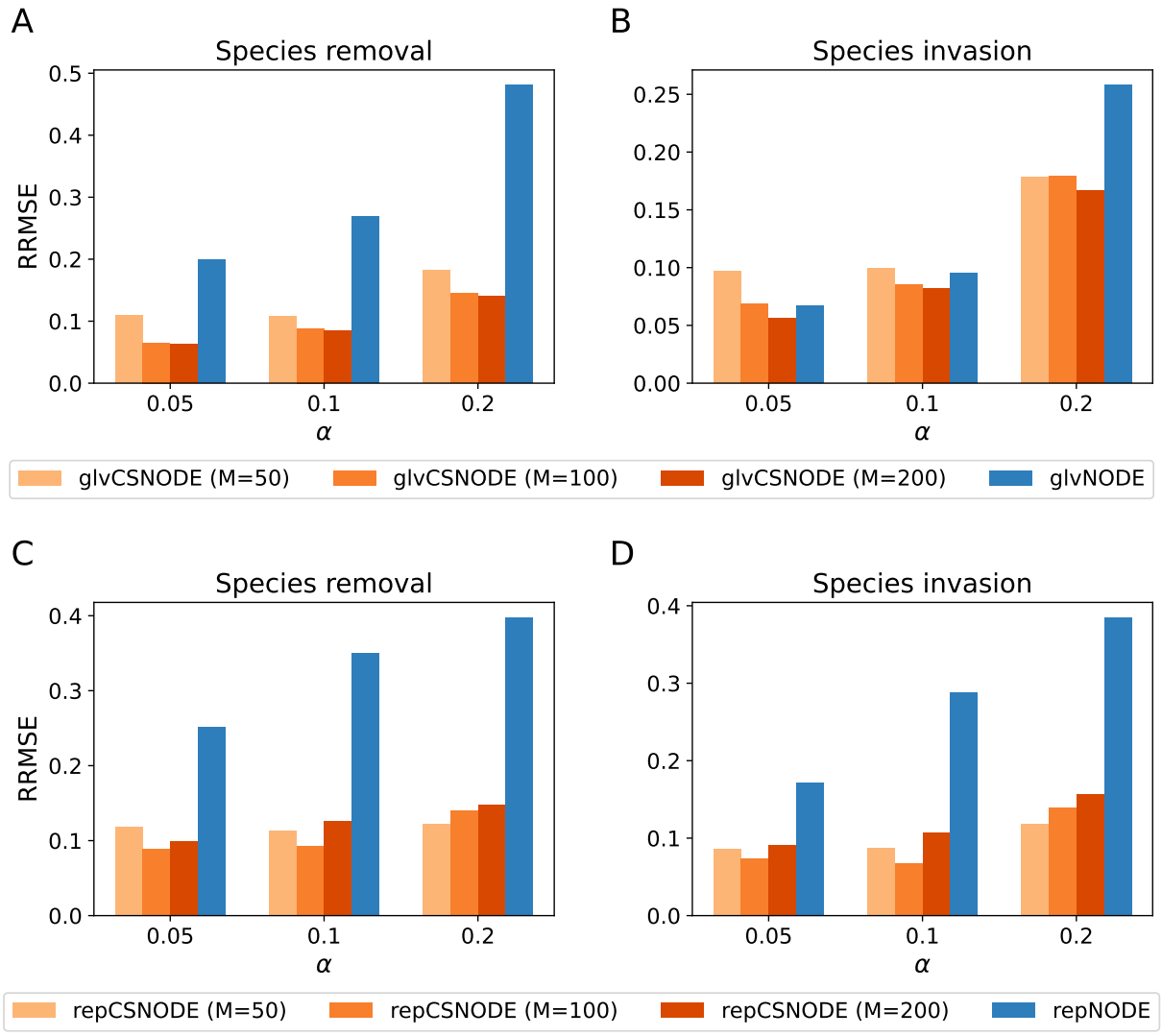

Figure S5: Prediction of perturbation responses on MiCRM-simulated data. (A, B) Mean RRMSE of glvCSNODE and glvNODE for species removal and species invasion, respectively. (C, D) Corresponding mean RRMSE of repCSNODE and repNODE. For the CSNODE-based methods, results are further stratified by the number of cross-sectional samples $m \in \{50, 100, 200\}$.

2 Alternative ways of introducing deviations from universality

To further assess robustness to perturbations, we additionally considered two alternative schemes:

- **Sparse perturbations.** A proportion π of the off-diagonal entries that were zero in the baseline matrix was randomly activated, with values drawn from $N(0, 0.1^2)$, matching the baseline interaction scale. To make this setting more stringent, we fixed the baseline sparsity level at $\rho = 0.6$.

- **Sign-flip perturbations.** A proportion r of the nonzero off-diagonal entries had their signs flipped. To ensure comparability with the sparse perturbation setting, we fixed $\rho = 0.4$, so that 60% of the off-diagonal entries were nonzero and thus eligible for perturbation.

3 Simulations based on the microbial consumer resource model

In the Microbial Consumer Resource Model (MiCRM), microbial growth depends on resource uptake and maintenance costs, while resource dynamics are jointly shaped by external supply, microbial consumption, and leakage-mediated byproduct production (Marsland et al. 2020). Specifically, microbial abundance C_i follows

$$\frac{dC_i}{dt} = C_i \left\{ (1-\lambda) \sum_{\alpha} \mu_{i\alpha} R_\alpha - m_i \right\},$$

and metabolite abundance R_α follows

$$\frac{dR_\alpha}{dt} = \rho_\alpha - \omega_\alpha R_\alpha - R_\alpha \sum_i \mu_{i\alpha} C_i + \lambda \sum_\beta l_{\alpha\beta} \left(R_\beta \sum_i \mu_{i\beta} C_i \right).$$

Here, $\mu_{i\alpha}$ denotes the resource consumption coefficient, m_i the maintenance cost, ρ_α the resource inflow, ω_α the dilution rate, $l_{\alpha\beta}$ the fraction of leaked flux from consumed resource β that is redistributed to metabolite α, and λ the leakage fraction.

Based on this model, we simulated microbial community dynamics and used the resulting abundance data to train repCSNODE and glvCSNODE. We then evaluated their ability to predict community responses to two types of perturbations, as outlined below.

3.1 Data simulation

The simulations were configured with a community size of $K = 15$, $d = 15$ metabolites, $n = 50$ time points, and a cross-sectional sample size of $m \in \{50, 100, 200\}$. All results were based on 100 independent simulation runs.

For each simulation replicate, we set leakage fraction $\lambda = 0.5$, maintenance cost $m_i = 0.4$, and $\omega_\alpha = 0.5$. The resource inflow parameters ρ_α were sampled from $U(0, 1)$. The consumption coefficient $\mu_{i\alpha}$ was sampled from a mixture distribution: with probability 0.2, $\mu_{i\alpha} \sim U(0, 5)$; and with probability 0.8, $\mu_{i\alpha} = 0$. The resulting consumption matrix was then normalized row-wise. The byproduct coefficient $l_{\alpha\beta}$ was sampled from a mixture distribution: with probability 0.5, $l_{\alpha\beta} \sim U(0, 1)$; and with probability 0.5, $l_{\alpha\beta} = 0$. The resulting byproduct matrix was then normalized column-wise.

Initial microbial abundances $\mathbf{C}_0$ and metabolite abundances $\mathbf{R}_0$ were sampled independently from $U(0, 1)$. The true abundance trajectories were obtained by numerically solving the MiCRM equations at time points $\{1, 2, \ldots, n\}$ using the `deSolve` package in R. Pre-perturbation noisy observations were then generated using the same procedure as in the

main text, with noise level $\alpha \in \{0.05, 0.1, 0.2\}$.

For cross-sectional steady-state data, the same setup was used with the following modifications: (1) a local community was defined by randomly selecting species indicators $z_i \in \{0, 1\}$, where the initial abundance C_{0i} was set to 0 whenever $z_i = 0$; and (2) the MiCRM equations were numerically integrated from the initial condition $(\mathbf{C}_0, \mathbf{R}_0)$ to a sufficiently large time point, $t = 1000$, yielding approximately steady-state samples.

We then generated post-perturbation datasets under two perturbation scenarios:

- **Species knockout.** For each $i \in \{1, 2, \ldots, K\}$, we set the abundance of species i at t_0 to zero, while keeping the abundances of all other microbial species and all metabolites unchanged. The resulting perturbed state was then used as the initial condition for MiCRM to generate n noisy post-perturbation observations, using the same noise levels as in the pre-perturbation data.

- **Species invasion.** We identified the least abundant microbial species at t_n and increased its abundance by an invasion inoculum equal to 10% of the total microbial abundance at that time point, while keeping the abundances of all other microbial species and all metabolites unchanged. The resulting perturbed state was then used as the initial condition for MiCRM to generate n noisy post-perturbation observations.

3.2 Prediction of perturbation responses on simulated data

Using the simulated pre-perturbation microbial observations, we trained glvNODE; glvCSNODE was trained by further incorporating cross-sectional samples. In parallel, repNODE and repCSNODE were trained on the corresponding relative-abundance data without and with cross-sectional samples, respectively.

For glvCSNODE and glvNODE, let $\mathbf{y}_i^{\text{pert}} \in \mathbb{R}^K$ denote the observed post-perturbation

microbial abundance vector at time point t_i, and let $\hat{\mathbf{y}}_i^{\text{pert}}$ denote the corresponding predicted abundance vector. Prediction performance was quantified by the relative root mean squared error (RRMSE)

$$\text{RRMSE}(\hat{\mathbf{y}}^{\text{pert}}) = \sqrt{\frac{\sum_{i=1}^{n} \left\| \hat{\mathbf{y}}_i^{\text{pert}} - \mathbf{y}_i^{\text{pert}} \right\|_2^2}{\sum_{i=1}^{n} \left\| \mathbf{y}_i^{\text{pert}} \right\|_2^2}}.$$

For repCSNODE and repNODE, we converted the observed post-perturbation microbial abundances into relative abundances before computing the RRMSE.

glvCSNODE consistently achieved lower RRMSE than glvNODE under species removal across all noise levels (Figure S5A). Under species invasion, the advantage of glvCSNODE depended on the cross-sectional sample size: at lower noise levels, glvCSNODE was slightly better than glvNODE when larger cross-sectional sample sizes were used, whereas at the highest noise level it outperformed glvNODE for all cross-sectional sample sizes (Figure S5B). In contrast, repCSNODE consistently outperformed repNODE under both species removal and species invasion (Figure S5C, D). Overall, these results show that incorporating cross-sectional data improves the prediction of post-perturbation community responses, with especially consistent gains for repCSNODE.

4 Application to experimental datasets

We applied repCSNODE to two human microbiome datasets, both of which provide microbial compositions in terms of relative abundances (David et al. 2014, Caporaso et al. 2011). Details of the bioinformatic processing are provided in Section 5. In parallel, we applied glvCSNODE to two datasets that provide absolute abundance measurements (Bucci et al. 2016, Lin et al. 2025). All four datasets were sampled at high frequency (nearly daily). To simplify model training, we approximated the time intervals between consecutive samples

as one day and set one day as the time unit.

We assessed model performance and reported quantitative stability metrics using cross-validation. Concretely, we fit the model on each training fold. The resulting model was then used to (1) compare the predictive performance of CSNODE-based methods with their corresponding NODE baselines through out-of-sample forecasting on the held-out fold, as described in the main text; (2) compute keystoneness consistently on the full dataset and quantify its stability using the mean pairwise Spearman rank correlation, as well as top-5 and top-10 overlap rates; and (3) for glvCSNODE, compute the selection frequency and sign consistency of each inferred interaction edge across folds.

4.1 repCSNODE reconstructs microbiome dynamics across lifestyle and infection transitions

Human associated microbial communities can undergo rapid and significant alterations due to routine human activities and exposures. To investigate how lifestyle and infection were associated with changes in the salivary and gut microbiota, we applied repCSNODE to longitudinal microbiome data collected over a 12-month period from Subject A and Subject B in a study by David et al. (2014). We modeled the two subjects separately to characterize subject-specific microbiome dynamics across distinct temporal phases.

4.1.1 repCSNODE infers the impact of lifestyle transitions in Subject A's microbiome dynamics

Subject A's samples span three distinct periods: (i) the pre-travel period spent in a major American metropolitan area (Days 1-70; 39 salivary samples and 65 gut samples), (ii) international travel to a Southeast Asian country (Days 71-122; 33 salivary samples and 40

Table 1: Cross-validation assessment of the stability of keystoneness rankings inferred under the repCSNODE model for microbiome data from Subject A and Subject B.

SubjectID	Body Site	Period	Spearman	Top-5 (%)	Top-10 (%)
A	Saliva	Pre-travel	0.436	61.8%	77.6%
A	Saliva	Travel	0.370	48.9%	79.8%
A	Saliva	Post-travel	0.526	57.3%	78.7%
A	Feces	Pre-travel	0.548	61.3%	77.1%
A	Feces	Travel	0.487	61.8%	80.9%
A	Feces	Post-travel	0.540	64.9%	79.3%
B	Feces	Pre-travel	0.339	59.6%	77.1%
B	Feces	Post-travel	0.454	70.7%	78.2%

gut samples), and (iii) the post-travel period following the return home (Days 123–364; 204 salivary samples and 218 gut samples). We focused our analysis on the 15 most abundant genera, constructing a separate repCSNODE model for each period using samples from all periods other than the current one as cross-sectional data.

We performed cross-validation by partitioning the samples within each temporal period into 10 contiguous, equally sized blocks. As shown in Figure S6A, repCSNODE consistently outperformed repNODE in trajectory prediction across all three temporal periods for both salivary and gut microbiota, underscoring the benefit of incorporating cross-sectional data into dynamic modeling. The inferred keystoneness rankings for Subject A exhibited moderate stability (mean Spearman: 0.370–0.548), while the top-ranked genera remained relatively consistent (top-5 overlap: 48.9%–64.9%; top-10 overlap: 77.1%–80.9%) (Table 1).

We then trained repCSNODE on all samples from each period for both salivary and gut microbiota. Subsequently, keystoneness scores were computed for each genus, and the top 5 genera in each period were identified as candidate keystone taxa. For the salivary microbiota, Figure S6B shows an interesting pattern: changes in living environment may

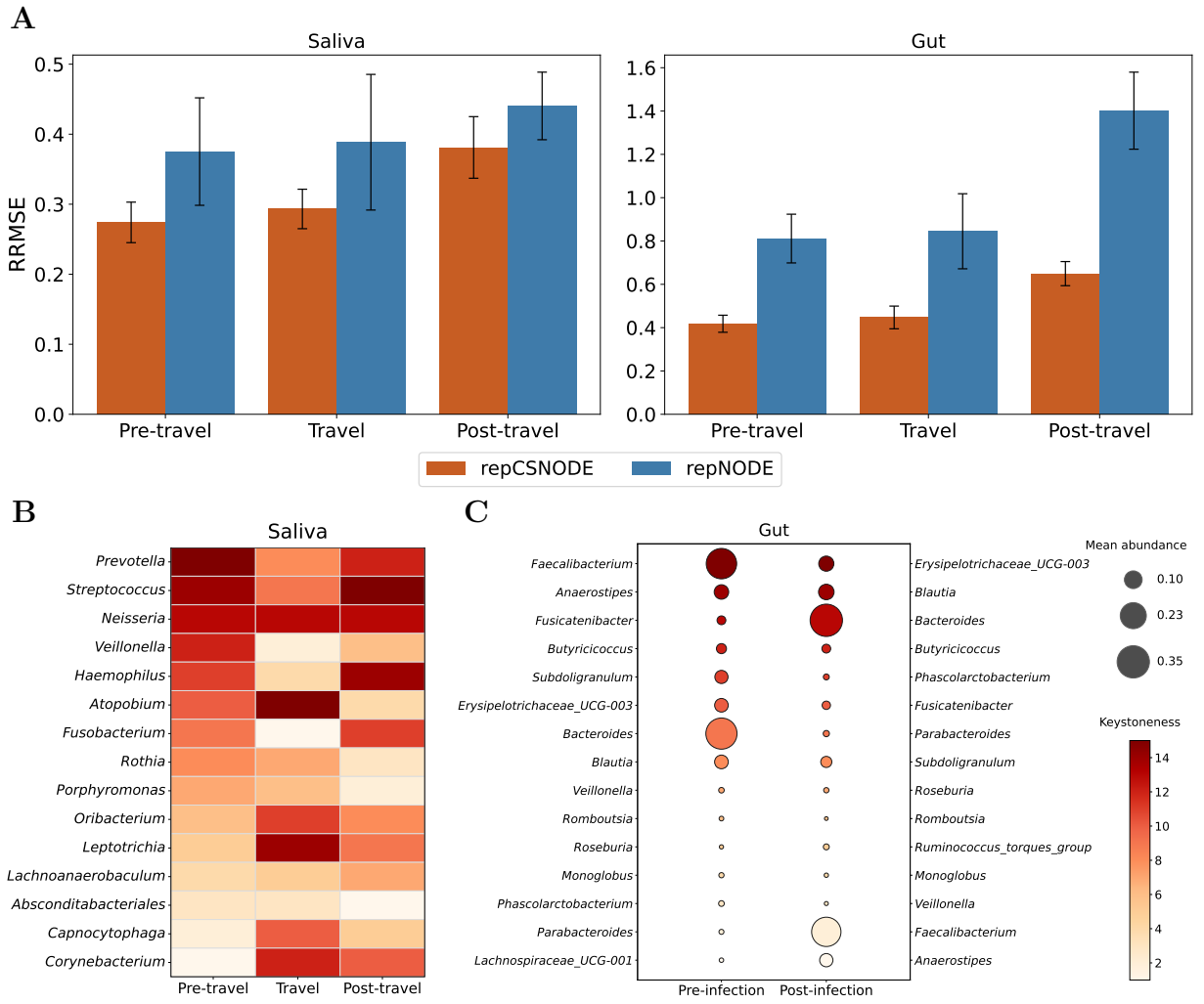

Figure S6: Analysis of longitudinal lifestyle microbiome data from Subject A. (A) Comparison of trajectory prediction performance between repCSNODE and repNODE on saliva and gut samples. Each bar shows the mean RRMSE from 10-fold cross-validation, with error bars representing the mean ± standard error of the mean. (B) Heatmap showing the ranks of keystoneness for saliva microbiota across three distinct time periods. (C) Bubble plot of keystoneness ranks for gut microbiota during the pre-travel and travel periods. Higher keystoneness ranks indicate greater ecological influence.

lead to alterations in the composition of candidate keystone taxa, but these changes appear to be reversible. Specifically, four genera, *Prevotella*, *Streptococcus*, *Neisseria*, and *Haemophilus*, were consistently identified as candidate keystone taxa in both the pre-travel

and post-travel periods. These taxa are well-established, functionally important members of the oral microbiome. For instance, *Streptococcus* and *Neisseria* are recognized as early colonizers that contribute to biofilm formation and nitrate reduction, respectively, while *Haemophilus* plays a role in mucosal immunity (Dieckow et al. 2024, Tseng et al. 2025).

In contrast, the candidate keystone taxa identified during the travel period were largely distinct from those in the pre- and post-travel periods, sharing only a single genus, *Neisseria*, in common. This persistent presence suggests that *Neisseria* may act as a resilient ecological component, maintaining its central role within the oral microbiota despite environmental perturbations. Notably, dietary patterns in Southeast Asia are typically characterized by a higher proportion of carbohydrate intake compared to those in the United States (Sikorski et al. 2023). Correspondingly, during the travel period, the genus *Leptotrichia* exhibited a marked increase in keystoneness rank relative to the pre- and post-travel periods. *Leptotrichia* is well known for its capacity to ferment carbohydrates, which may explain its elevated ecological importance under the carbohydrate-rich dietary conditions experienced abroad (Thompson & Pikis 2012).

Furthermore, we examined the impact of international travel on the candidate keystone genera of the gut microbiota. As shown in Figure S6C, three genera, *Faecalibacterium*, *Anaerostipes*, and *Butyricicoccus*, were identified as candidate keystone taxa shared between the pre-travel and travel periods. These genera are known butyrate producers that play crucial roles in maintaining intestinal homeostasis, modulating host immune responses, and contributing to anti-inflammatory effects within the gut ecosystem (Lopez-Siles et al. 2017, Bui et al. 2021, Geirnaert et al. 2014). This finding suggests that the core structure of butyrate-producing bacteria in the gut is largely preserved despite short-term environmental perturbations such as travel.

Interestingly, although the genus *Bacteroides* maintained relatively high abundance during the travel period, its keystoneness rank exhibited a marked decline. *Bacteroides* has been widely associated with Western-style diets that are high in fat and protein (Gorvitovskaia et al. 2016). The observed decrease in its ecological importance coincided with the subject's transition to a non-Western dietary environment, typically characterized by lower fat and protein intake. This highlights the sensitivity of our keystoneness metric to ecologically meaningful dietary shifts.

4.1.2 repCSNODE captures infection transition dynamics in Subject B's microbiome

Subject B provided gut samples across three clinical periods: (i) the pre-infection period (Days 1-150; 121 gut samples), (ii) the acute *Salmonella* infection period (Days 151-159; 7 gut samples), and (iii) the post-infection convalescent period (Days 160-252; 58 gut samples). The *Salmonella* infection caused a persistent shift in gut microbiota composition, without reversion to the pre-infection state (David et al. 2014). Owing to the limited number of samples collected during the infection phase, these data were treated as cross-sectional, and no period-specific model was constructed for this interval.

For Subject B, we used the same cross-validation scheme as for Subject A. As shown in Figure S7A, while repCSNODE outperformed repNODE in the pre-infection period, it exhibited slightly inferior performance in the post-infection period. This discrepancy may be due to the drastic restructuring of the gut microbiota induced by infection, which rendered the pre-infection and infection period samples unsuitable as cross-sectional data to enhance repCSNODE in the post-infection period. The inferred keystoneness rankings for Subject B also showed moderate stability across cross-validation folds (Table 1).

We then trained repCSNODE on all samples from each period and computed keystone-

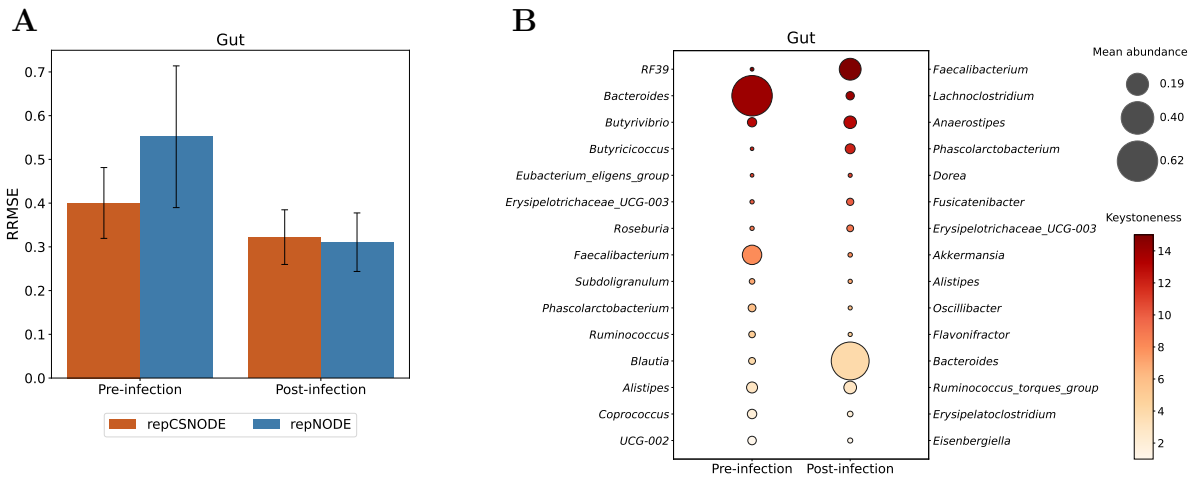

Figure S7: Analysis of longitudinal lifestyle microbiome data from Subject B. (A) Comparison of trajectory prediction performance between repCSNODE and repNODE. Each bar shows the mean RRMSE over 10-fold cross-validation, with error bars indicating mean ± standard error of the mean. (B) Bubble plot of keystoneness ranks for gut microbiota during the pre-infection and post-infection periods. Higher keystoneness ranks indicate greater ecological influence.

ness scores for each genus. As shown in Figure S7B, the top five candidate keystone taxa identified in the pre-infection and post-infection periods shared no overlapping genera. However, most of these candidate keystone taxa in both periods were short-chain fatty acid (SCFA) producers. This suggests that, although the infection led to a significant shift in gut microbial composition, the identified candidate keystone taxa remained closely associated with maintaining core metabolic functions. Such a pattern indicates structural complementarity within the microbial community, which may help preserve overall functional stability.

4.2 repCSNODE suggests keystone taxa and their potential roles in skin microbiomes

To further investigate dynamic differences in microbial communities across body sites within the same individual and between individuals, we analyzed skin microbiome data from two healthy participants in a longitudinal study (Caporaso et al. 2011). In this dataset, Subject F4 (female) contributed 134 left palm samples and 133 right palm samples, while Subject M3 (male) provided 365 left palm samples and 359 right palm samples. For each palm of each subject, we selected the top 15 most abundant genera and constructed palm-specific models. Notably, this dataset offered naturally paired samples, two skin sites (left and right palms) from the same individual. We treated samples from one palm as cross-sectional data when building the repCSNODE model for the other palm.

Given the large sample size, we divided the samples from each palm into 30 contiguous, equally sized blocks and performed cross-validation. As shown in Figure S8A, repCSNODE consistently achieved the lowest prediction errors and demonstrated more stable performance compared to repNODE. The inferred keystoneness rankings showed moderate stability across cross-validation folds (Table 2; mean Spearman: 0.528–0.614), while the top-ranked genera remained relatively consistent (top-5 overlap: 63.9%–70.6%; top-10

Table 2: Cross-validation assessment of the stability of keystoneness rankings inferred under the repCSNODE model for longitudinal palm microbiome data.

SubjectID	Body Site	Spearman	Top-5 (%)	Top-10 (%)
M3	L_Palm	0.568	70.6%	79.3%
M3	R_Palm	0.563	63.9%	80.6%
F4	L_Palm	0.528	64.5%	79.2%
F4	R_Palm	0.614	68.3%	80.1%

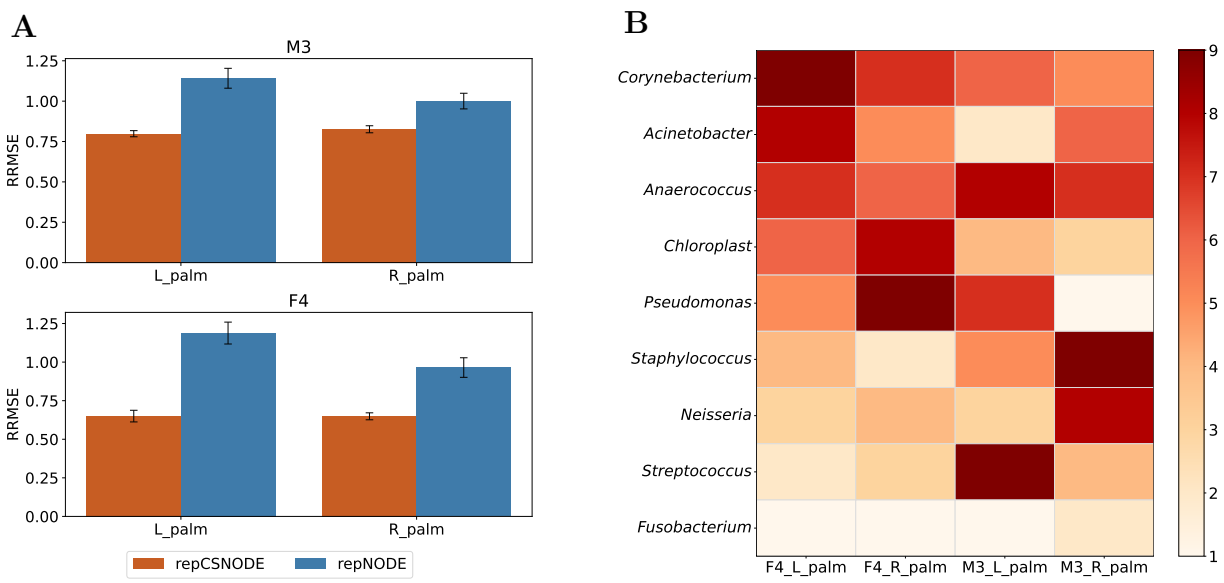

Figure S8: Analysis of longitudinal palm microbiome data from two individuals. (A) Comparison of trajectory prediction performance between repCSNODE and repNODE for subjects F4 and M3. Each bar shows the mean RRMSE across 30-fold cross-validation, with error bars indicating mean ± standard error of the mean. (B) Ranks of keystoneness for genera shared between palms and across individuals; larger values indicate greater ecological influence.

overlap: 79.2%–80.6%).

We next trained repCSNODE using all available samples from each palm, using the paired palm data from the same individual as cross-sectional data. We then computed keystoneness scores of the genera shared between the two individuals to quantify their influence on microbial community dynamics. The ranks of the shared nine genera are shown in Figure S8B. The top five genera with the highest scores were identified as candidate keystone taxa.

For subject F4, the candidate keystone taxa were identical on both palms: *Corynebacterium*, *Acinetobacter*, *Anaerococcus*, *Chloroplast*, and *Pseudomonas*. With the exception of *Chloroplast*, the other genera are known to play key roles in skin microbial ecology (Ridaura et al. 2018, Fyhrquist et al. 2014, van der Krieken et al. 2023, Wu et al. 2011). In

contrast, subject M3 shared only two candidate keystone taxa between the left and right palms: *Corynebacterium* and *Anaerococcus*. This suggests that, despite frequent physical contact between the hands, notable ecological differences in the skin microbiome can persist, consistent with the findings of Caporaso et al. (2011). The larger difference in candidate keystone taxa between M3's palms, compared to the minimal difference in F4, may be attributable to distinct hand-usage behaviors.

Moreover, *Anaerococcus* and *Corynebacterium* were shared as candidate keystone taxa in both F4 and M3, and both are known to play important roles in regulating skin immunity. Specifically, members of the genus *Corynebacterium* have been shown to influence local skin immunity by stimulating IL17A producing T cells in the dermis (Ridaura et al. 2018). Likewise, *Anaerococcus*, a representative of Gram-positive anaerobic cocci, can enhance the skin's antimicrobial defense by triggering host cells to produce antimicrobial peptides and other protective responses (van der Krieken et al. 2023). These findings suggest that the presence of these candidate keystone taxa reflects conserved functional roles in maintaining skin homeostasis and defending against pathogenic invasion.

4.3 glvCSNODE infers dietary fiber effects on probiotic colonization

A probiotic cocktail composed of *Clostridia* strains with regulatory T cell–inducing capacity has been proposed as a potential therapeutic approach for inflammatory bowel disease (Bucci et al. 2016). However, gut microbial communities are highly sensitive to environmental perturbations, particularly changes in dietary fiber intake, which can markedly alter their composition and function (O'Keefe et al. 2015). Understanding how different dietary fiber conditions perturb probiotic candidate interaction patterns and reshape the

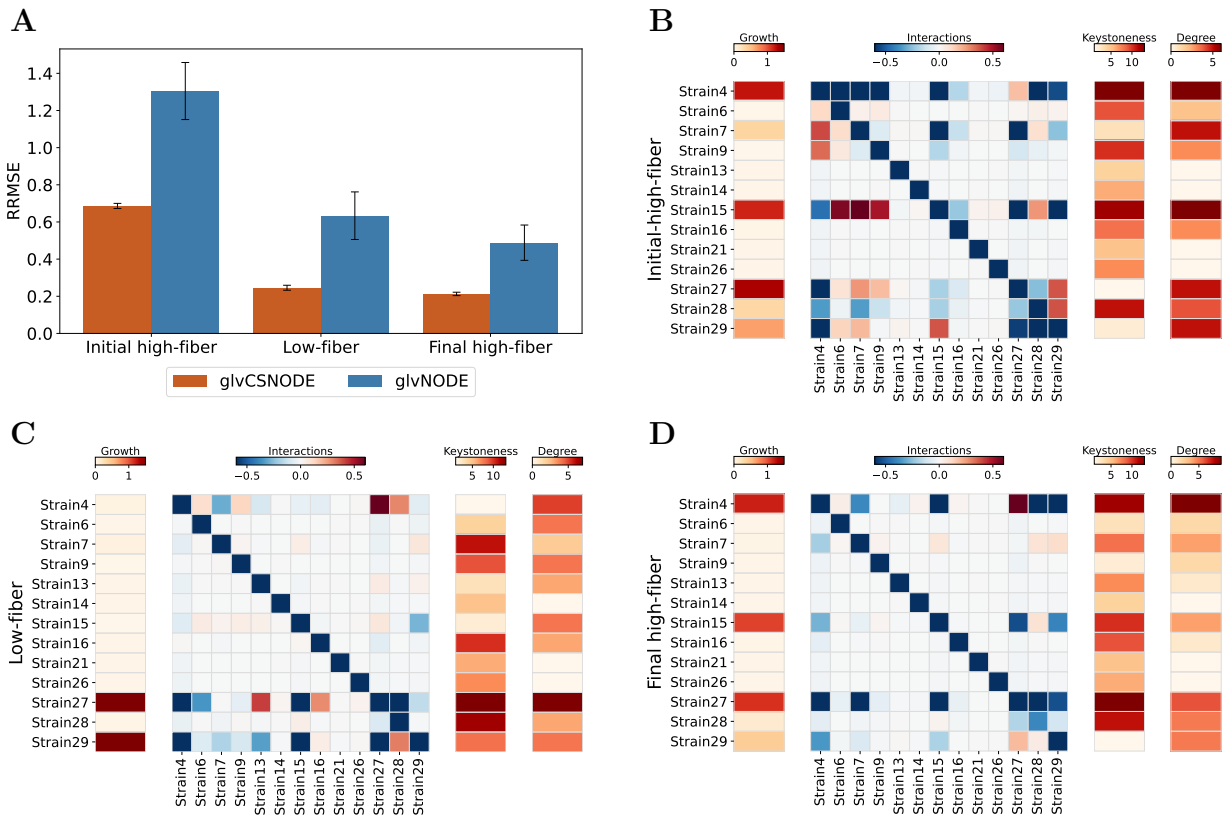

Figure S9: Analysis of the probiotic colonization dataset under dietary fiber perturbations. (A) Trajectory prediction performance of glvCSNODE and glvNODE across different dietary phases. Bars represent the mean RRMSE from cross-validation, with error bars indicating the mean ± standard error of the mean. (B-D) Inferred ecological networks and keystoneness ranks for (B) the initial high-fiber phase, (C) the low-fiber phase, and (D) the final high-fiber phase. For each strain we report (i) intrinsic growth rates (values exceeding 1.5 were clipped for visualization); (ii) interaction parameters (values clipped to –0.6 to 0.6 for visualization); (iii) keystoneness rank (larger values indicate greater ecological influence); and (iv) network degree.

ecological roles of candidate keystone species may yield valuable insights into both microbial ecology and inform the design of diet-compatible probiotic therapies.

Here, we applied glvCSNODE to a probiotic colonization dataset, in which a mixture of 13 strains was orally inoculated into seven germ-free adult mice (Bucci et al. 2016). Two mice remained on a high-fiber diet for 5 weeks, while the other five underwent a dietary

shift from high-fiber diet (5 weeks) to low-fiber diet (2 weeks) and then back to high-fiber diet (2 weeks). For each dietary phase, we constructed a separate gvlCSNODE model, treating samples from the other phases as cross-sectional data.

We first performed hold-one-subject-out cross-validation. glvCSNODE consistently outperformed glvNODE across all three dietary phases (Figure S9A). The distribution of selection frequencies showed a clear separation between frequently selected edges and rarely selected edges, indicating a stable core subset of candidate interaction patterns (Figure S10). The corresponding scatter plots further demonstrated high sign consistency, with many edges falling into the robust region. The inferred keystoneness rankings showed high stability across cross-validation folds, while the top-ranked strains remained highly consistent (Table 3).

We next applied glvCSNODE to infer microbial interaction networks using the complete set of samples from each dietary phase. Based on the inferred models, we computed keystoneness scores to quantify phase-specific ecological influence and network degrees to assess strain-level connectivity. The inferred growth rates, interaction parameters, keystoneness ranks, and network degrees for the 13 strains are presented in Figures S9B–D. For each dietary phase, the strain with the highest keystoneness rank exhibited greater connectivity in the inferred interaction network, indicating that our dynamic keystoneness

Table 3: Cross-validation assessment of the stability of keystoneness rankings inferred under the glvCSNODE model for the probiotic colonization dataset.

Intervention	Spearman	Top-5 (%)	Top-10 (%)
Initial high-fiber	0.948	89.5%	95.2%
Low-fiber	0.760	86.0%	90.0%
Final high-fiber	0.814	88.0%	96.0%

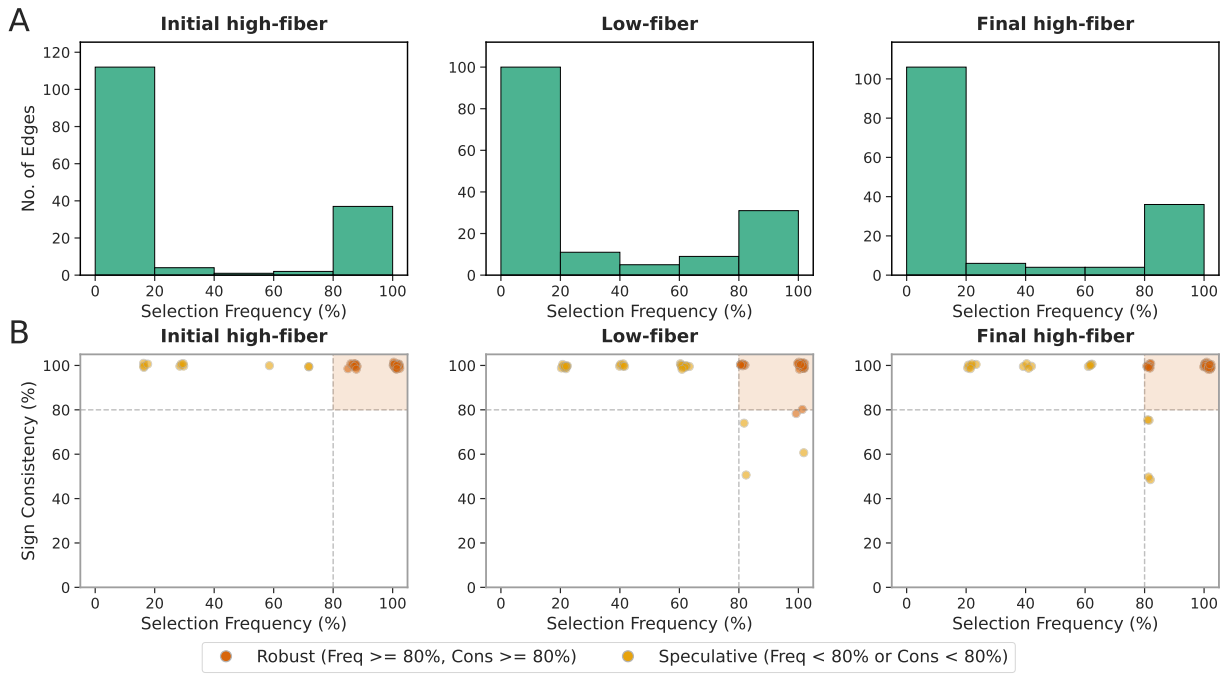

Figure S10: Cross-validation stability of inferred interaction edges across different dietary phases. The estimated interaction matrix was first converted into a binary network as described in the main text. The selection frequency and sign consistency of each edge were then computed. Interactions with both selection frequency and sign consistency exceeding 80% were classified as robust. (A) Distribution of edge selection frequency across folds. (B) Selection frequency versus sign consistency for edges selected in at least one fold, shown for the three dietary intervals.

metric identifies species that occupy central roles within the microbial community.

Comparing keystoneness ranks across dietary phases (Figure S11), strains 4 and 15 ranked highly during both high-fiber phases but much lower during the low-fiber phase. Strain 15, closely related to *Clostridium asparagiforme*, is known to efficiently ferment dietary fiber and produce short-chain fatty acids (Bucci et al. 2016). In contrast, strain 28 maintained both high keystoneness and strong network connectivity across all phases, suggesting that it functions as a resilient ecological hub.

Together, these results suggested that glvCSNODE improved trajectory prediction and

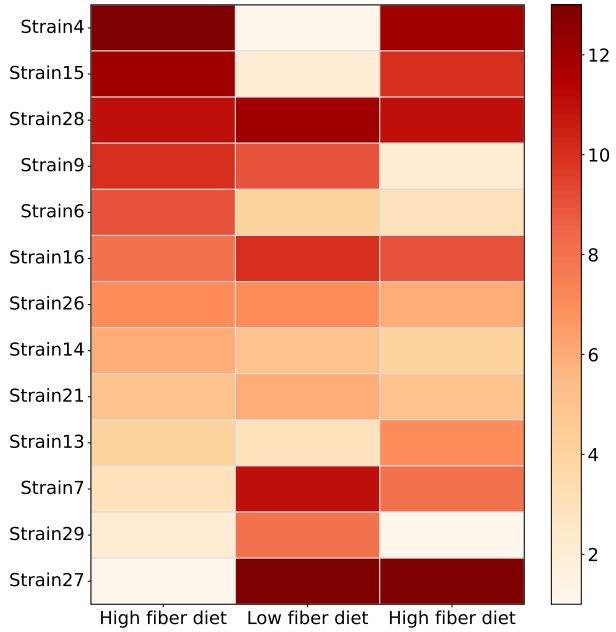

Figure S11: Analysis of the probiotic colonization dataset under dietary fiber perturbations. Heatmap showing the ranks of keystoneness across the three dietary phases, larger values indicate greater ecological influence.

helped characterize phase-specific microbial candidate interaction patterns across dietary conditions. Moreover, the dynamic keystoneness metric highlighted species that may play influential roles in the community response to dietary perturbations.

4.4 glvCSNODE suggests interaction patterns in the human gut microbiome

Given the limitations of gnotobiotic mouse models in fully capturing the complexity and ecological realism of human gut microbiota, we sought to gain deeper insight into microbe-microbe interactions under physiologically relevant conditions by analyzing a densely sampled dataset from a human dietary fiber trial (Lin et al. 2025). This dataset comprised daily fecal samples from 19 overweight individuals: 10 without type 2 diabetes (T2D) and 9 with T2D. Each participant followed a sequential dietary regimen consisting of a two-week

Table 4: Cross-validation assessment of the stability of keystoneness rankings inferred under the glvCSNODE model for the human dietary fiber intervention dataset.

Group	Intervention	Spearman	Top-5 (%)	Top-10 (%)
Overweight	Habitual	0.863	89.3%	88.2%
Overweight	Low-dose	0.898	80.4%	93.6%
Overweight	High-dose	0.849	92.0%	86.2%
T2D	Habitual	0.940	91.7%	93.1%
T2D	Low-dose	0.616	68.9%	87.2%
T2D	High-dose	0.887	92.2%	91.9%

habitual diet, one week of low-dose fiber supplementation, and one week of high-dose fiber supplementation. We focused on the 15 most abundant species, and constructed separate models for each dietary phase within each group. Samples from other dietary phases within the same group were used as cross-sectional samples during model training.

We first performed hold-one-subject-out cross-validation. glvCSNODE consistently outperformed glvNODE across all three dietary phases in both the Overweight and T2D groups (Figure S12A). Across conditions, the lowest selection-frequency bin contained the largest proportion of edges, indicating that many candidate interactions were consistently not selected (Figure S13). At the same time, under the habitual diet, a subset of edges exhibited high selection frequency and strong sign consistency, suggesting a relatively stable interaction structure prior to intervention. Following intervention, selection frequencies became more dispersed and sign consistency decreased, particularly in the T2D group, leading to a reduction in the number of robust edges. Overall, these results indicated that only a subset of inferred interactions was consistently supported across data perturbations, and that stronger perturbations were associated with reduced stability and an increased proportion of speculative edges. The keystoneness rankings remained relatively stable across

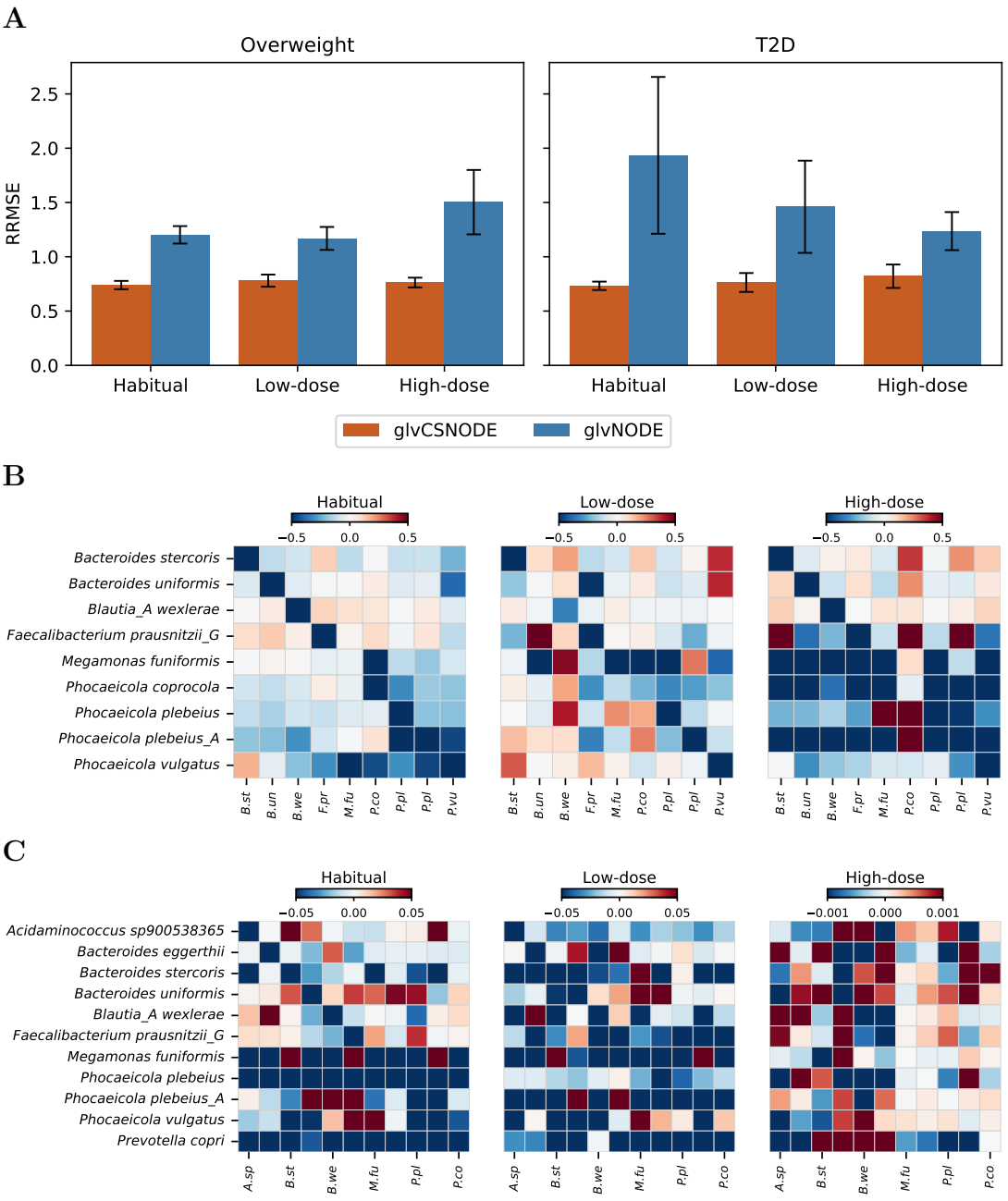

Figure S12: Analysis of the human gut microbiome dataset under dietary fiber interventions. (A) Comparison of trajectory prediction performance between glvCSNODE and glvNODE. Each bar represents the mean RRMSE across cross-validation, with error bars indicating the mean ± standard error of the mean. (B–C) Inferred interaction networks for (B) the Overweight group and (C) the T2D group, showing only microbial species shared across all three phases. Interaction values were clipped for visualization.

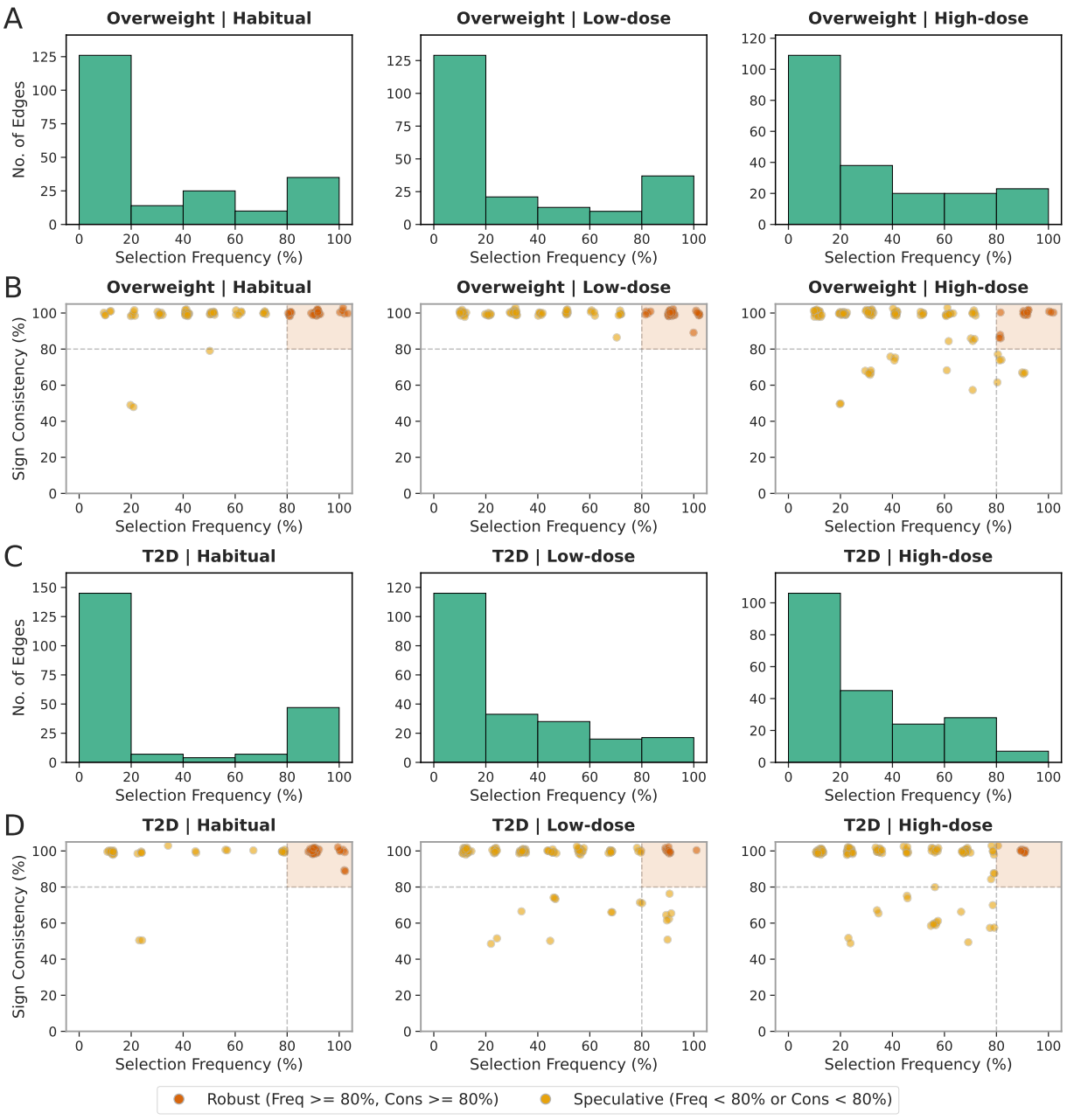

Figure S13: Cross-validation stability of inferred interaction edges. The estimated interaction matrix was first converted into a binary network as described in the main text. The selection frequency and sign consistency of each edge were then computed. Interactions with both selection frequency and sign consistency exceeding 80% were classified as robust. (A, C) Distribution of edge selection frequency across folds for the Overweight and T2D groups, respectively. (B, D) Selection frequency versus sign consistency for edges selected in at least one fold across the three dietary periods.

cross-validation folds (Table 4).

We next trained glvCSNODE using all available samples from each dietary phase. Given that the inferred interaction edges were less stable across conditions, the resulting interaction networks suggest phase-specific candidate interaction patterns rather than definitively uncovering them. As shown in Figures S12B, C, dietary fiber intervention led to notable alterations in inferred interaction networks within both groups. In the Overweight group, fiber intake increased cooperative interactions targeting *Bacteroides stercoris*, *Bacteroides uniformis* and *Phocaeicola vulgatus* compared to the habitual diet. These species are known for their anti-obesity effects, suggesting that dietary fiber may promote their proliferation through enhanced microbial cooperation (Ryu et al. 2024, Fabersani et al. 2021, Wen et al. 2024). However, under the high-dose fiber condition, *Phocaeicola vulgatus* exhibited a higher number of competitive interactions compared with the low-dose phase, indicating that increased fiber intake does not universally enhance microbial cooperation.

In the T2D group, dietary fiber trial also promoted cooperative interactions, particularly toward *Bacteroides stercoris* and *Phocaeicola vulgatus*. This restructuring of interactions likely created a more favorable environment for species with anti-obesity effects. These findings align with Lin et al. (2025), who observed body weight reductions in both groups following fiber supplementation. Moreover, *Prevotella copri*, a species with antidiabetic potential (Yang et al. 2024), experienced reduced competitive pressure and increased cooperations with other microbes.

To further quantify the ecological influence of shared species, we computed their keystoneness scores (Figure S14). With increasing fiber dosage, *Faecalibacterium prausnitzii_G* became more influential in the Overweight group, while *Bacteroides stercoris* increased in influence in the T2D group. Both species are associated with body weight reduction, sug-

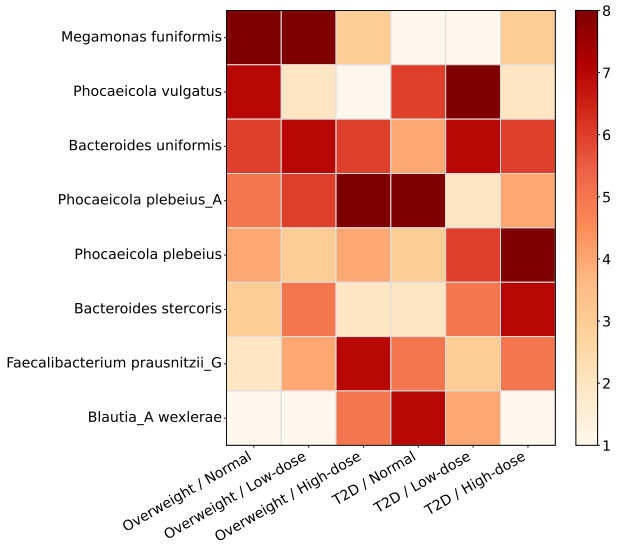

Figure S14: Analysis of the human gut microbiome dataset under dietary fiber interventions. Shown are shared candidate keystone species across groups and dietary phases, ranked by keystoneness scores. Higher values indicate greater ecological influence.

gesting that fiber supplementation enhanced ecological importance of these species within their respective microbial communities (Yang et al. 2023, Fabersani et al. 2021). Additionally, in the T2D group, *Bacteroides uniformis* showed increased keystoneness following fiber supplementation, suggesting an enhanced central role in microbial network dynamics that could contribute to improved metabolic outcomes.

Together, these results suggested that glvCSNODE not only improved trajectory prediction but also helped characterize microbial interaction patterns and identify species that may be ecologically influential in response to dietary fiber interventions.

5 Bioinformatic processing of sequences

Sequencing data were processed using QIIME 2 (Version 2023.2). DADA2 was first applied for denoising, effectively removing sequencing errors and generating both the feature ta-

ble and representative sequences. Phylogenetic trees were then constructed by performing multiple sequence alignment with MAFFT, followed by rapid tree generation using FastTree. Taxonomic classification was performed with a classifier trained on the SILVA 138 database. OTUs present in less than 1% of samples were filtered out.

References

Bucci, V., Tzen, B., Li, N., Simmons, M., Tanoue, T., Bogart, E., Deng, L., et al. (2016), 'MDSINE: Microbial dynamical systems inference engine for microbiome time-series analyses', *Genome Biology* **17**, 121.

Bui, T. P. N., Mannerås-Holm, L., Puschmann, R., Wu, H., Troise, A. D., Nijsse, B., Boeren, S., et al. (2021), 'Conversion of dietary inositol into propionate and acetate by commensal Anaerostipes associates with host health', *Nature Communications* **12**, 4798.

Caporaso, J. G., Lauber, C. L., Costello, E. K., Berg-Lyons, D., Gonzalez, A., Stombaugh, J., Knights, D., et al. (2011), 'Moving pictures of the human microbiome', *Genome Biology* **12**, R50.

David, L. A., Materna, A. C., Friedman, J., Campos-Baptista, M. I., Blackburn, M. C., Perrotta, A., Erdman, S. E., et al. (2014), 'Host lifestyle affects human microbiota on daily timescales', *Genome Biology* **15**, R89.

Dieckow, S., Szafrański, S. P., Grischke, J., Qu, T., Doll-Nikutta, K., Steglich, M., Yang, I., et al. (2024), 'Structure and composition of early biofilms formed on dental implants are complex, diverse, subject-specific and dynamic', *npj Biofilms and Microbiomes* **10**, 155.

Fabersani, E., Portune, K., Campillo, I., López-Almela, I., la Paz, S. M.-d., Romaní-

Pérez, M., Benítez-Páez, A., et al. (2021), 'Bacteroides uniformis CECT 7771 alleviates inflammation within the gut-adipose tissue axis involving TLR5 signaling in obese mice', *Scientific Reports* **11**(1), 11788.

Fyhrquist, N., Ruokolainen, L., Suomalainen, A., Lehtimäki, S., Veckman, V., Vendelin, J., Karisola, P., et al. (2014), 'Acinetobacter species in the skin microbiota protect against allergic sensitization and inflammation', *Journal of Allergy and Clinical Immunology* **134**(6), 1301–1309.

Geirnaert, A., Steyaert, A., Eeckhaut, V., Debruyne, B., Arends, J. B., Van Immerseel, F., Boon, N., et al. (2014), 'Butyricicoccus pullicaecorum, a butyrate producer with probiotic potential, is intrinsically tolerant to stomach and small intestine conditions', *Anaerobe* **30**, 70–74.

Gorvitovskaia, A., Holmes, S. P. & Huse, S. M. (2016), 'Interpreting Prevotella and Bacteroides as biomarkers of diet and lifestyle', *Microbiome* **4**, 15.

Lin, X., Wang, C., Liu, B., Zhu, Y., Zhai, R. & Zhang, C. (2025), 'Temporal response patterns of human gut microbiota to dietary fiber', *iMeta* **4**, e70046.

Lopez-Siles, M., Duncan, S. H., Garcia-Gil, L. J. & Martinez-Medina, M. (2017), 'Faecalibacterium prausnitzii: from microbiology to diagnostics and prognostics', *The ISME Journal* **11**(4), 841–852.

Marsland, R., Cui, W. & Mehta, P. (2020), 'A minimal model for microbial biodiversity can reproduce experimentally observed ecological patterns', *Scientific Reports* **10**, 3308.

O'Keefe, S. J. D., Li, J. V., Lahti, L., Ou, J., Carbonero, F., Mohammed, K., Posma,

J. M., et al. (2015), 'Fat, fibre and cancer risk in African Americans and rural Africans', *Nature Communications* **6**, 6342.

Ridaura, V. K., Bouladoux, N., Claesen, J., Chen, Y. E., Byrd, A. L., Constantinides, M. G., Merrill, E. D., et al. (2018), 'Contextual control of skin immunity and inflammation by Corynebacterium', *Journal of Experimental Medicine* **215**(3), 785–799.

Ryu, S. W., Moon, J. C., Oh, B. S., Yu, S. Y., Bak, J. E., Heo, E. S., Jeong, J.-H., et al. (2024), 'Anti-obesity activity of human gut microbiota Bacteroides stercoris KGMB02265', *Archives of Microbiology* **206**(1), 19.

Sikorski, C., Yang, S., Stennett, R., Miller, V., Teo, K., Anand, S. S., Paré, G., et al. (2023), 'Changes in energy, macronutrient, and food consumption in 47 countries over the last 70 years (1950-2019): a systematic review and meta-analysis', *Nutrition* **108**, 111941.

Thompson, J. & Pikis, A. (2012), 'Metabolism of sugars by genetically diverse species of oral Leptotrichia', *Molecular Oral Microbiology* **27**, 34–44.

Tseng, Y.-C., Liao, K.-S., Lin, W.-T., Li, C., Chang, C.-B., Hsu, J.-W., Chan, C.-P., et al. (2025), 'A human oral commensal-mediated protection against Sjögren's syndrome with maintenance of T cell immune homeostasis and improved oral microbiota', *npj Biofilms and Microbiomes* **11**, 18.

van der Krieken, D. A., Rikken, G., Ederveen, T. H., Jansen, P. A., Rodijk-Olthuis, D., Meesters, L. D., van Vlijmen-Willems, I. M., et al. (2023), 'Gram-positive anaerobic cocci guard skin homeostasis by regulating host-defense mechanisms', *iScience* **26**(4), 106483.

Wen, X., Feng, X., Xin, F., An, R., Huang, H., Mao, L., Liu, P., et al. (2024), 'B. vul-

gatus ameliorates high-fat diet-induced obesity through modulating intestinal serotonin synthesis and lipid absorption in mice', *Gut Microbes* **16**(1), 2423040.

Wu, D. C., Chan, W. W., Metelitsa, A. I., Fiorillo, L. & Lin, A. N. (2011), 'Pseudomonas skin infection: clinical features, epidemiology, and management', *American Journal of Clinical Dermatology* **12**(3), 157–169.

Yang, C., Lan, R., Zhao, L., Pu, J., Hu, D., Yang, J., Zhou, H., et al. (2024), 'Prevotella copri alleviates hyperglycemia and regulates gut microbiota and metabolic profiles in mice', *mSystems* **9**(7), e00532–24.

Yang, M., Wang, J.-H., Shin, J.-H., Lee, D., Lee, S.-N., Seo, J.-G., Shin, J.-H., et al. (2023), 'Pharmaceutical efficacy of novel human-origin Faecalibacterium prausnitzii strains on high-fat-diet-induced obesity and associated metabolic disorders in mice', *Frontiers in Endocrinology* **14**, 1220044.